Imaging coseismic rupture in far field by slip patches

M. Vallée* and M. Bouchon

Laboratoire de Géophysique Interne et Tectonophysique, Observatoire de Grenoble, Université Joseph Fourier, 38000 *Grenoble, France.*
E-mail: mvallee@obs.ujf-grenoble.fr

SUMMARY

Since the end of the 1970s, teleseismic waves are used routinely to infer the first-order characteristics of the event (location, depth, duration, focal mechanism), but finding the second-order kinematic parameters (spatial distribution of slip, rupture velocity and more basically the discrimination between the fault plane and the other nodal plane) of distant events remains a difficult task. Classically, these events are studied by two different methods; either they are seen as a succession of subevents, each of which is considered as a point source, or like in near field, as extended sources where the kinematic parameters are retrieved on a grid. The first approach is not physically satisfactory and can lead to erroneous interpretations of the rupture process (Ihmlé 1998) while the second one often gives highly non-unique results. In this work, we present a method that aims to find a simplified source model able to explain the main features of the teleseismic data. The basic idea is to consider the event as an ensemble of slip patches, breaking at different rupture velocities. In order to obtain a simple and stable model, we use a maximum of two slip patches and model only periods longer than a third/fourth of the earthquake global duration. We use three different types of data: *P* and *SH* body waves through direct modelling, and surface waves through an empirical Green function (EGF) technique. We follow a recent efficient approach to stabilize the EGF deconvolutions with physical constraints. The method is applied to the 1999 Izmit (Turkey) and 1995 Jalisco (Mexico) earthquakes and gives results consistent with previous studies of these events. Thanks to its simplicity, this method can be applied almost routinely after each large earthquake, and can give interesting insights on the physical properties of the rupture (size, slip, rupture velocity) as well as important clues on the risk associated with the event (for example tsunami risk).

Key words: empirical Green function, far field, Izmit, Jalisco, non-linear inversion, seismic source kinematics.

1 INTRODUCTION

Since the emergence of centroid determinations (Backus 1977), this method has been the most widely used tool to retrieve the basic properties of an earthquake. When an earthquake above M_W 5.5 occurs, location, depth, magnitude and focal mechanism can be quickly and reliably determine5 with the global networks (Harvard centroid moment tensor, Dziewonski *et al.* 1981). Nevertheless, for many reasons, it is useful to study the more refined characteristics of the event. Physically, the centroid model is not satisfactory, because all the radiated energy is mapped into one point whereas it is clear that this energy is spread. Such a simple model is not able to show how earthquake rupture propagates. Tectonically, we would like to know at least which plane of the focal mechanism is the fault plane and to have an estimate of the size of the fault. Finally, in some applications, we need to know the spatial distribution of slip along

the fault: for example, modelling tsunamis caused by earthquakes requires the knowledge of the coseismic slip close to the ocean bottom.

This is why a lot of effort has been made, with different types of data, to infer the higher order characteristics of earthquake kinematics. Since the 1971 San Fernando earthquake and more importantly the 1979 Imperial Valley earthquake (Archuleta 1982; Olson & Apsel 1982; Hartzell & Heaton 1983), near field data are included when the earthquake occurs inland in a well-instrumented area. This allows detection of small-scale details of the rupture (down to 5 km) but it is important to have a large network of stations to retrieve the global behaviour of the fault because the stations are highly influenced by the nearest feature of the source process. GPS measurements, INSAR interferometry (Massonnet *et al.* 1993) and more recently SPOT data (Michel & Avouac 2002) are also used in inland areas to infer the static displacements caused by earthquakes. Combinations of these technics are of course possible and sometimes used (e.g. Hernandez *et al.* 1999; Delouis *et al.* 2002). Nevertheless, none of these data allows a systematic analysis of the earthquakes as teleseismic data do: no matter where the earthquake

*Now at: Laboratoire de Détection Géophysique, CEA, BP12, 91680 Bruyéres-Le Chătel, France.

occurs, inland or offshore, in a well instrumented area or not, it is always recorded, with a good azimuthal coverage, by a similar number of distant stations.

In the proceeding sections, we shall first discuss the current methods which aim to improve the centroid models with teleseismic data. We illustrate the fact that a real source tomography is often too ambitious a goal except in extremely well instrumented areas. This is why we propose a global method—based on the representation of coseismic rupture by slip patches—to identify the most robust features of large earthquake source processes. We start from simple uniform models and allow complication of such models only if the data clearly requires it. Applications to widely studied earthquakes (1999 Izmit, Turkey; 1995 Jalisco, Mexico) will finally be shown.

2 METHODS CURRENTLY USED TO RETRIEVE THE SPATIAL EXTENSION OF THE RUPTURE

2.1 Second order of the moment tensor

First, it is possible to use directly the high order information of the moment tensor as described, for example, by Bukchin (1995) or McGuire *et al.* (2001), based on the early work of Backus (1977). It is assumed that the event has a constant mechanism, i.e. the time derivative of the stress glut m can be written:

$$\dot{m}_{jk}(\boldsymbol{\xi}, \tau) = \dot{f}(\boldsymbol{\xi}, \tau)\mathcal{M}_{jk}, \tag{1}$$

where, $\mathcal{M}$ is a constant unit moment tensor, f is a scalar function, and $\boldsymbol{\xi}$ and τ denote the space and time dependencies. At low frequencies, we can write the far field displacement component $U_i(\mathbf{x}, t)$ produced by an earthquake as:

$$U_i(\mathbf{x}, t) = \frac{1}{M_0}\left(M_0 + f^{(0,1)}(\tau_s)\frac{\partial}{\partial \tau} + \mathbf{f}^{(1,0)}(\boldsymbol{\xi}_s).\nabla_\mathbf{s} + \frac{1}{2}f^{(0,2)}(\tau_s)\frac{\partial^2}{\partial \tau^2}\right.$$
$$\left. + \boldsymbol{f}^{(1,1)}(\boldsymbol{\xi}_s, \tau_s)\frac{\partial}{\partial \tau}.\nabla_\mathbf{s} + \frac{1}{2}\boldsymbol{f}^{(2,0)}(\boldsymbol{\xi}_s):\nabla_\mathbf{s}\nabla_\mathbf{s}\right)\tilde{s}(\mathbf{x}, t, \boldsymbol{\xi}_s, \tau_s), \tag{2}$$

where $\tilde{s}(\mathbf{x}, t, \boldsymbol{\xi}_s, \tau_s)$ denotes the displacement produced by a point source in $(\boldsymbol{\xi}_s, \tau_s)$ of the same mechanism and same global moment M_0. Eq. (2) makes use of the spatiotemporal moments $f^{(i,j)}$ of $\dot{f}$ relative to an origin $(\boldsymbol{\xi}_s\tau_s)$, which has to be chosen close to the hypocentre of the earthquake:

$$f^{(0,0)} = \int_{-\infty}^{\infty} d\tau \int_{V_s} d^3\xi \, \dot{f}(\boldsymbol{\xi}, \tau) = M_0 \tag{3}$$

$$f_i^{(1,0)}(\boldsymbol{\xi}_s) = \int_{-\infty}^{\infty} d\tau \int_{V_s} d^3\xi \, \dot{f}(\boldsymbol{\xi}, \tau)(\xi_i - \xi_{si}) \tag{4}$$

$$f^{(0,1)}(\tau_s) = \int_{-\infty}^{\infty} d\tau \int_{V_s} d^3\xi \, \dot{f}(\boldsymbol{\xi}, \tau)(\tau - \tau_s) \tag{5}$$

$$f_{ij}^{(2,0)}(\boldsymbol{\xi}_s) = \int_{-\infty}^{\infty} d\tau \int_{V_s} d^3\xi \, \dot{f}(\boldsymbol{\xi}, \tau)(\xi_i - \xi_{si})(\xi_j - \xi_{sj}) \tag{6}$$

$$f_i^{(1,1)}(\boldsymbol{\xi}_s, \tau_s) = \int_{-\infty}^{\infty} d\tau \int_{V_s} d^3\xi \, \dot{f}(\boldsymbol{\xi}, \tau)(\xi_i - \xi_{si})(\tau - \tau_s) \tag{7}$$

$$f^{(0,2)}(\tau_s) = \int_{-\infty}^{\infty} d\tau \int_{V_s} d^3\xi \, \dot{f}(\boldsymbol{\xi}, \tau)(\tau - \tau_s)^2. \tag{8}$$

The first moments $f^{(0,1)}$ and $\boldsymbol{f}^{(1,0)}$ are related to the temporal and spatial centroids of the rupture, whereas the second moments $f^{(0,2)}$, $\boldsymbol{f}^{(1,1)}$ and $\boldsymbol{f}^{(2,0)}$ are related to three characteristic parameters

of the rupture: the longitudinal extension, the downdip extension and the average rupture velocity (see for example Bukchin 1995 for the relationships between these parameters).

By such a study, it becomes possible to discriminate the two focal planes and gain an idea of the spatial and temporal extents of the rupture. Nevertheless, the obtained values are difficult to relate with the reality of the rupture: for example, the characteristic dimensions cannot be directly interpreted as the real rupture size. A refinement of this method was proposed by Dahm & Krüger (1999): the idea is to use the Taylor developments not around the global rupture centroid but around several centroids distributed between the beginning and the end of the rupture. By doing so, it becomes possible to model higher frequency waveforms.

Yet, observations of teleseismic waveforms show some coherent high frequency details that should allow us to obtain a non-uniform distribution of slip or rupture velocity on the fault. The following methods are usually used to retrieve these characteristics.

2.2 Subevent analysis

The most common improvement of the point-source model is to consider that the rupture is constituted of several point sources, generally called subevents. The most classical way to do such an analysis is to retrieve the relative-source time functions for each considered station. This can be done by deconvolving the signals from a theoretical Green function (e.g. Kikuchi & Kanamori 1982) or from an empirical Green function (EGF) (e.g. Velasco *et al.* 1994a). Through the analysis of the time-shifts (Fukao 1972) between some well identified peaks in the relative-source time functions, the locations of the subevents on the fault can be obtained.

This method often leads to a satisfactory fit to the data but the physical interpretation of these subevents, in terms of location of the moment release, is difficult. As shown by Ihmlé (1998) for the 1994 deep Bolivia earthquake, these subevents do not have to be a place of high moment release but are only representative of the instantaneous centroid of this moment release; typically, if the rupture front is circular, all the subevents will be around the centre of the circle (see the instructive fig. 10 in Ihmlé's paper). A direct interpretation of the location of these subevents would lead to the erroneous conclusion that this part of the fault broke several times. This can explain why numerous subevent analyses present this dubious characteristic of rerupturing some parts of the fault. Although this phenomenon is of course theoretically possible, some inversions in the near field where this possibility is allowed, tend to show that it happens only marginally (Das & Kostrov 1990, 1994). Lastly, the rupture velocity, found by the time shifts between subevents, will be underestimated for the same reason: when a subevent is identified at a time t_0, it does not mean that the rupture front is at this location at this time t_0. At this time t_0, the rupture front will be generally further from the hypocentre than the subevent.

This is why, even in the far field, a real extended image of the fault is useful to retrieve some physical insights of the rupture process.

2.3 Extended source

The goal of this method, introduced by Olson & Apsel (1982) and Hartzell & Heaton (1983), is to reproduce what happened on the fault during the earthquake. The fault is usually discretized into subfaults and the kinematic parameters, classically slip s, onset time T and rise time d are retrieved for each subfault. Each subfault is itself represented by an array of point sources which must be fine enough to mimic a continuous rupture propagation. The spectral displacement U at a station is simply given by a sum over the n

point sources, with the appropriate time and space shifts. It can be written:

$$U(\omega) = \sum_{j=1}^{n} G(\omega, z_j) f_j^l(\omega) e^{i(\mathbf{k}.\mathbf{l_j} - \omega T_j)}, \tag{9}$$

where

(i) $G(\omega, z_j)$ represents the ground motion for a unit moment point source at a depth z_j with a given source mechanism

(ii) $f_j^l(\omega)$ is the local spectral source time function which depends on slip s_j and rise time d_j

(iii) $\mathbf{k}$ is the horizontal wavenumber

(iv) $\mathbf{l}_j$ is the horizontal space shift between the hypocentre and point source j

(v) . is the scalar product

(vi) T_j is the time of rupture propagation between the hypocentre and point source j.

Theoretically, by solving an inverse problem, the kinematic parameters can be retrieved at each point of the fault. Nevertheless, the main problem with this type of analysis is its high non-uniqueness (Das & Kostrov 1994). One of the main difficulties concerns the size of the grid: to be able to retrieve high frequency details in the rupture history, we have to use a fine enough grid. Yet, high frequencies are dominated by lower frequencies (see the simple Haskell model which gives an ω^2 law or other more refined laws) and trying to model small details makes the problem unstable. To reduce this instability, we can either use larger subfaults, or keep small subfaults and introduce a smoothing parameter. Neither method is really satisfactory: the first one completely forbids the modelling of detail, yielding a very smooth model and a relatively poor fit; while the second one leads to a trade-off between the size of the grid and the smoothing parameter. Resolution limits of these detailed analyses, particularly if the event is complex, are also shown by comparing the various results obtained for the recent 1999 Chi-Chi (Taiwan) earthquake (Ma *et al.* 2001; Zeng & Chen 2001; Wu *et al.* 2001) or 1999 Izmit (Turkey) earthquake, for which the various inverted models gathered by Clévédé *et al.* (2004) (Fig. 1) show the high variability of the results. This instability can also be partly understood
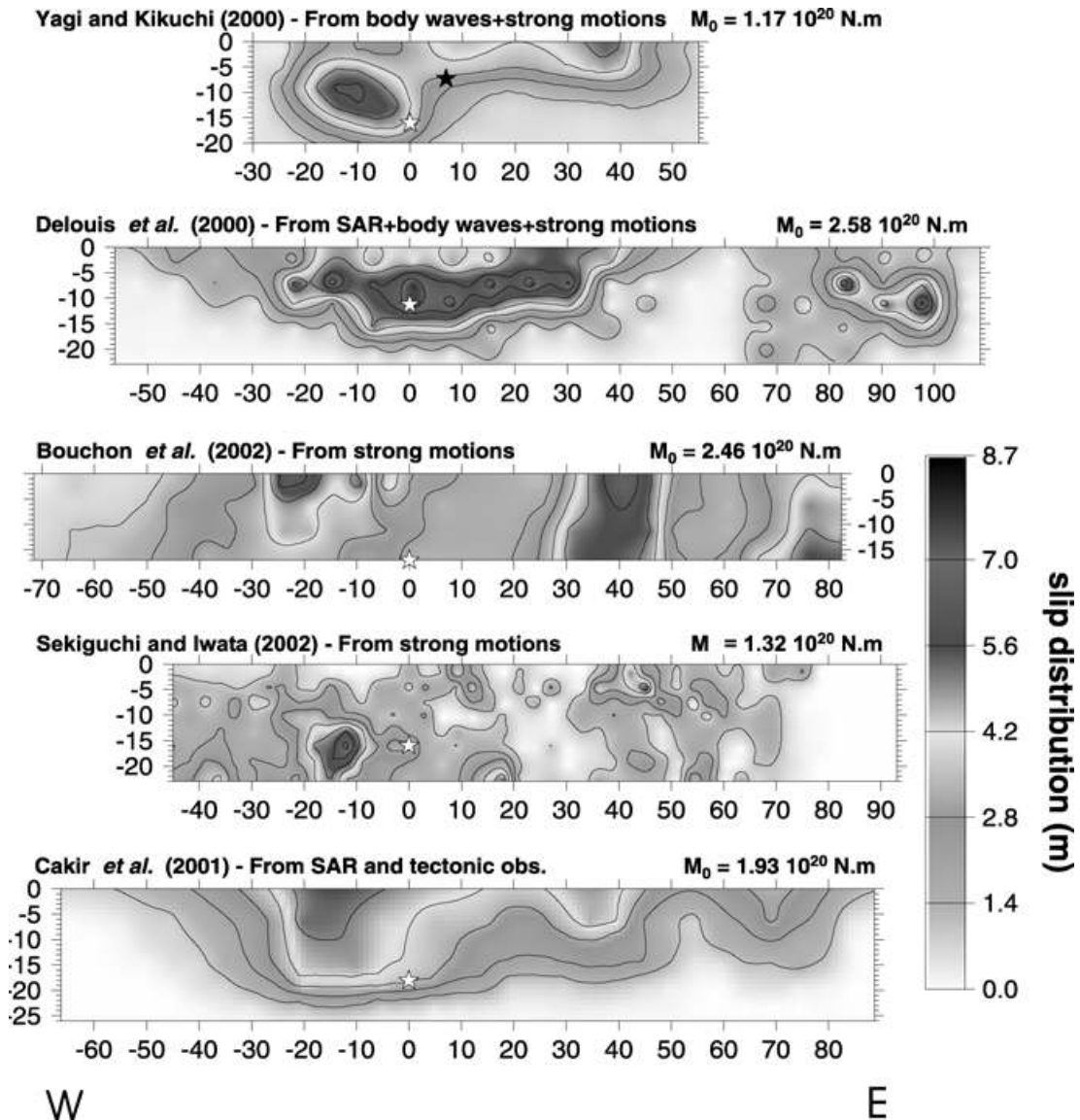

Figure 1. Figure adapted from Clévédé *et al.* (2004): Five inversion results for the slip distribution of the 1999 August 17 Izmit (Turkey) earthquake are presented. This figure illustrates the high variability of the details of the rupture process in the case where only a few accelerometers are present.

by considering that some poorly known parameters, such as precise fault geometry (Das & Suhadolc 1996), hypocentral depth and exact mechanism, are extremely important in the retrieval of the precise source process.

3 SLIP PATCH METHOD

3.1 General description

The idea of the method presented here is to keep an extended representation of the source so that the model has a physical meaning, but to obtain a more robust solution than the one coming from the classical discretization of the fault into subfaults. We plan to construct a source model giving more information than a centroid approach without doing a real source tomography. To do so, we propose to model an earthquake by one or two slip patches, rupturing at possibly different velocities. Simple or relatively small earthquakes will be described by a unique slip patch, whereas other events will require the addition of another slip patch. Of course, even when represented with two slip patches, we only propose a very simplified image of the reality of an earthquake. Nevertheless, we justify our modelling by different observations:

(i) As mentioned before, attempts to really explain all the details of the rupture are not really reliable, particularly in the general case where there are no or only a few near field accelerograms. Yet, in most cases, we can see that there are some large-scale details that are constant from one model to the other: in the case of the Taiwan event, a 60 km long northward rupture propagation with an average slip of 6–8 m; in the case of the Izmit event, a bilateral rupture with a main slip zone of about 70 km. We aim to represent this type of detail and in the following paragraphs we show that our approach enables this.

(ii) The study of Thatcher (1990) (see in particular fig. 3 in the referenced article), which gathers a number of results of the main features of different kinematic inversions, shows also what was reliably resolved: typically one, two or three slip patches. Other studies often focus on the main slip zone or main asperity of an earthquake,

which is responsible for a large part of the waveforms and therefore is the most resolvable feature of the source (e.g. Ihmlé & Ruegg 1997; Ma *et al.* 2000; Abercrombie *et al.* 2001). In our method, such a model will be simply described by two slip patches: one describing some slip at the hypocentre, and a larger slip patch elsewhere on the fault describing the main slip zone.

(iii) Addition of a third, fourth, fifth, . . . patch yields an increasingly complicated inverse problem, and parallelly, searched details become increasingly difficult to identify.

(iv) This method of modelling has different practical advantages that will be discussed further, namely: few parameters, no need of a smoothing parameter, possibility of largely oversizing the fault in the starting model, possibility of inverting simultaneously the first-order kinematic parameters (hypocentral depth and focal mechanism) if their first determinations do not seem satisfactory.

(v) Finally, this is a simple modelling method that is generally able to explain the data with a good approximation. This simplicity criteria is researched in all source kinematics inversions, when smoothing is used to regularize the solution.

This approach will not allow us to explain the rupture very physically, because the parametrization is too restrictive. But we will be able to determine the size of the zone which has been ruptured, the part of the fault which has slipped the most and more basically which one of the two nodal planes is the fault plane. We can also obtain insights on the rupture velocity, because slip patches will be allowed to rupture at different velocities, and thus zones of high or slow rupture velocities are potentially resolvable.

In the following three subsections, we will describe more precisely how we parametrize an earthquake with this slip patch method, what data we use and lastly how we solve the inverse problem.

3.2 Parametrization of an earthquake

We consider that the fault is constituted of p patches and that each patch $\mathcal{P}_k$ has a constant slip s_k, constant local rise time d_k and constant rupture velocity Vr_k ($1 \leq k \leq p$). The precise parametrization is detailed in Fig. 2 in the two-patch model case: we need two
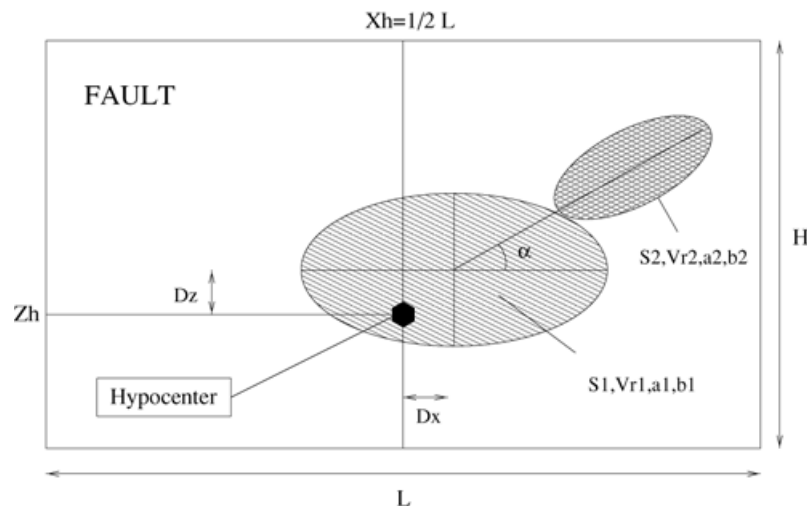

Figure 2. Description of the rupture process by two slip patches. Both patches have an elliptical shape and the first slip patch contains the hypocentre of the earthquake. 11 parameters are necessary to describe the rupture in this modelling: space shift between hypocentre and centre of the first slip patch (two parameters, noted Dx and Dz); slip, rupture velocity, large and small axis of the ellipses (four parameters for each patch – S_i, Vr_i, a_i, b_i); and finally an angle noted α which describes the position of the second patch compared to the centre of the first one. The lateral position of the hypocentre X_h is chosen in the middle of the fault and does not reduce the generality of the problem. Its vertical position Zh, like the focal mechanism, is assumed to have been determined previously, for example by the use of the one-patch model. The fault, parametrized by its length L and height H, is largely oversized and does not limit the extent of the rupture process.

parameters to describe the shift of the first patch centre compared to the hypocentre; four parameters to describe the first patch itself [geometry of the patch is represented as an ellipse (two parameters), slip and rupture velocity]; and finally, five parameters to describe the second patch [the same four parameters as for the first patch and another one to describe the position of the second patch compared to the first one (angle α)]. The rise times d_k are not inverted because of the usual low resolution of this parameter (e.g. Ihmlé 1996) and we simply fix them to values smaller than the periods considered in the inversion. This yields a total of 11 parameters, which keeps the inverse problem manageable (see the corresponding section).

In the simpler one-patch model case, we do not consider the five parameters related to the second patch, but we usually try to refine the focal mechanism and hypocentral depth of the earthquake. Therefore, in this case we model the earthquake by 10 parameters [focal mechanism (three), hypocentral depth (one), dimensions of the patch (two), position of the hypocentre (two), slip (one) and rupture velocity (one) inside the patch]. We do not give here the possibility of an oblique orientation of the slip patch. This could be done, but we consider that the freedom in the hypocentre position inside the patch is already able to partially reproduce this effect. Moreover, if such a long oblique rupture propagation is really necessary to explain the data, a two-patch model could then be used.

To compute the body *P*- and *SH*-wave teleseismic displacements, we still consider a subfault grid and use a modification of eq. (9), where we now sum on the p patches $\mathcal{P}_k (\Delta \leq k \leq p)$:

$$U(\omega) = \sum_{k=1}^{p} f_k^l(\omega) \sum_{j \in \mathcal{P}_k} G(\omega, z_j) e^{i(\mathbf{k} \cdot \mathbf{I}_j - \omega T_j)}. \tag{10}$$

The term $G(\omega, z_j)$ is computed using the reciprocal approach of Bouchon (1976). The 1-D crustal effects, both in the source and receiver crusts, are modelled by the reflectivity method (Müller 1985). Different crustal models will be considered depending on the source and station location. We used the global model Crust 5.1 of Mooney *et al.* (1998) to infer the Moho depths and obtain the regional source models. This formalism allows modelling of the complete direct *P* and *SH* wavefield, including the depth phases pP, sP and sS. The reflected core phases PcP and ScS, which may slightly interfere with the late part of the direct waves, are here neglected. The mantle propagation is classically modelled by the geometrical spreading and an attenuation term (parametrized by the usual t*, taken equal to 0.7 s for *P* waves and 2.8 s for *S* waves). A global model (IASP91) is used to infer the take-off angles below the crusts.

Finally, the onset times T_j are calculated given the values of $(Vr_k; 1 \leq k \leq p)$ by the finite difference scheme of Podvin & Lecomte (1991). This scheme was already used in this respect by Herrero (1994) and an application to a source study can be found in Vallée *et al.* (2003). This modelling allows the different patches to have different slip amounts and different rupture velocities. Contrary to eq. (9), we do not sum on the n point sources of the fault but only on the points of the fault which have experienced some slip. This allows us to largely oversize the fault without making the forward modelling too slow.

In our study of surface waves (see next section), we are interested in the relative source time function (RSTF), noted F_θ: this is the source time function distorted by the fact that we observe it through one station, i.e. in one particular direction. It can be written:

$$F_\theta(t) = \sum_{k=1}^{p} \sum_{j \in \mathcal{P}_k} f_j^l(t - T_j + D_j(\theta)/v_\phi), \tag{11}$$

where

(i) v_ϕ is the phase velocity surface wave. Due to the dispersion of these waves, an average value must be chosen, which is dependent on the dominant frequencies of the RSTF and of the source velocity structure. Eq. (11) shows also that the surface waves velocities outside the source region do not play a role in the RSTFs interpretation. This is simply due to the fact that these velocities affect similarly the EGF and the main shock.

(ii) D_j is the relative distance between the hypocentre and a point j, which is determined on the fault by its horizontal and vertical coordinates x_j and z_j. Given the azimuth θ of the station, the strike azimuth θ_F of the fault and the dip δ_F of the fault, this relative distance can be written:

$$D_j(\theta) = x_j \cos(\theta - \theta_F) + z_j \cot(\delta_F) \cdot \sin(\theta - \theta_F). \tag{12}$$

In this method, our goal is to retrieve the simplest model able to explain the data. This is why we will first try to explain the data with a single patch and we will add another patch only if the agreement with the data is not satisfactory. The use of a single patch model is also useful because, in this simple case, we can also simultaneously determine the first-order rupture parameters, such as the hypocentral depth and the focal mechanism. Subsequently, these values are considered known if we want later to refine the model with a second patch. Generally, we do not try to complicate the model with a third, fourth... patch because the searched details become less and less well-resolved. Thus, we prefer to limit the study to relatively long periods (typically one third or one fourth of the global rupture time) which generally leads to a satisfactory agreement with the observations using at most two patches.

3.3 Data used

3.3.1 Body waves

Body *P* and *SH* waves, at epicentral distances between 30° and 90° are often used in teleseismic source analysis. Their mantle propagation, essentially in the homogeneous lower mantle, is in fact easy to model and allows observation of any source effects. Moreover, today it is very easy and fast, through the use of IRIS-GEOSCOPE networks, to retrieve the waveforms. In this study, we will use vertical *P* displacements and transverse *SH* displacements, obtained by integration of the broad-band velocity records. To take into account the various instrumental responses of the stations, we deconvolve the data from their instrumental responses and then convolve them with a common bandpass filter (the high frequency corner is generally chosen as one third to one fourth of the earthquake global duration *D* and the low frequency corner is chosen equal to 0.0125 Hz). The time after the first *P*- or *SH*-wave arrival that we consider, depends on the duration *D* of the earthquake, which can be estimated by the prior use of surface waves (see next paragraph). Time windows have to be chosen longer for *SH* waves than for *P* waves to take into account lower frequencies and stronger directivity effects.

3.3.2 Empirical Green function technique for surface waves

Surface waves are difficult to use in detailed source studies except if we choose an EGF approach. As a matter of fact, the direct theoretical approach does not allow modelling of periods shorter than *ca* 30 s, because of the complicated structure of the first hundred kilometers of the Earth, and these are precisely the periods which are interesting to constrain the source process. The EGF analysis is used in seismology since the work of Hartzell (1978). The idea is
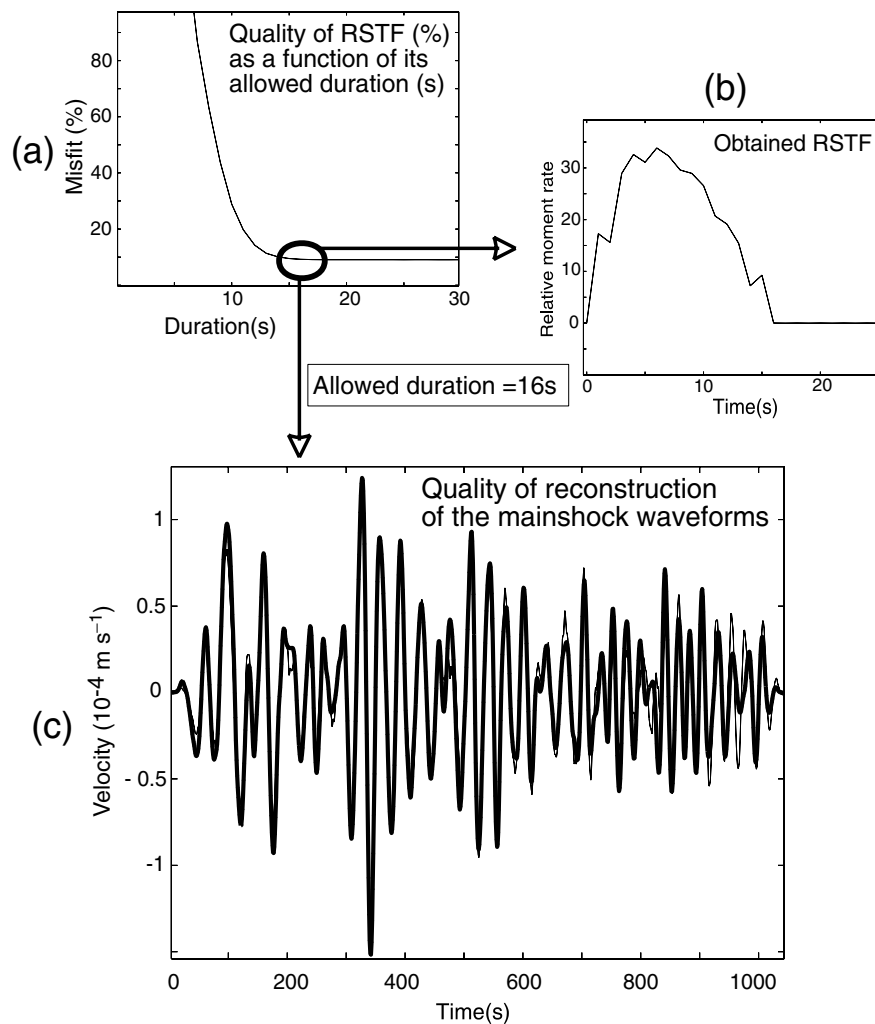
Figure 3. Illustration of the deconvolution technique for Love waves of the Izmit earthquake recorded at station KDAK. Deconvolution is done with the four physical constraints (causality, positivity, borned duration, and constant moment ratio fixed to 350.). First, we impose a very short duration of the RSTF which of course leads to a very bad reconstruction of the main shock waveforms by reconvolution with the EGF. The error associated with this reconstruction is our definition of the misfit used in (a). Then, we allow a longer and longer duration which decreases the misfit (a). When we reach an allowed duration of 16 s, the misfit is low (9 per cent), and cannot be improved further by a longer allowed duration. Therefore, we choose this 16 s long RSTF, presented in (b), as our selected RSTF. The convolution of this RSTF with the EGF yields the thin line in (c) whereas the thick line is the real main shock waveform.

to find a similar but smaller event in the vicinity of the main shock. By deconvolving the main shock from EGF waveforms at several stations, we retrieve the RSTFs of the main shock.

It may happen that no suitable EGF exists for a given earthquake. In this case, the slip patch method can be applied with body waves alone, but the obtained results will not be as reliable as with the complete analysis. As a matter of fact, the lateral rupture extension and the horizontal rupture velocity will be less well resolved because surface waves are much more sensitive to these parameters than body waves. Moreover, by using an EGF approach, we intrinsically separate the source effects from the propagation effects.

Different descriptions, applications and developments of the EGF analysis can be found in Velasco *et al.* (1994b), Courboulex *et al.* (1997b) or Schwartz (1999). A recent improvement was proposed by Bertero *et al.* (1997) using the physical constraints of the RSTF through an approach called the projected Landweber method to stabilize the deconvolution and to retrieve a more reliable RSTF. Namely, they used the positivity, the causality and the borned support properties of the RSTF. We have extended their method (Vallée

2004) to take into account a fourth constraint on the RSTF: the area of the RSTFs, which represents the ratio between the main shock and the EGF moments, has to remain constant for all stations, that is:

$$\int_{-\infty}^{\infty} F_\theta(t)\,dt = \frac{M_{\mathrm{MAIN}}}{M_{\mathrm{EGF}}}. \tag{13}$$

This physical constraint is very useful in the waveform inversion of RSTFs. If all RSTFs do not have the same area, they intrinsically cannot be fitted by our forward modelling in which this physical constraint is naturally respected. Quality of the constrained RSTFs can be simply evaluated by the quality of the reconstruction of the main shock waveform by convolution with the EGF. Practically, we will consider RSTFs leading to a variance reduction of the main shock reconstruction better than 65–70 per cent.

The method requires calculation of the RSTFs twice: first, we do not impose the moment constraint and then, based on the relative moments inferred by the best RSTFs, we recalculate the RSTFs with

this new constraint. We are choosing precisely the relative moment between the two earthquakes with the highest values among the best RSTFs, because we show in Vallée (2004) that moments are generally underestimated in presence of noise. These values are generally lower than the Harvard CMT inferred values because we can only explain the part of the main shock which is consistent with the EGF. For example, if there is a slight change of the mechanism during rupture, the moment involved in this part of the rupture process will be partly lost in the deconvolution.

As an example of the application of the technique, we present in Fig. 3 the EGF analysis at station KDAK for the Izmit earthquake (see the section concerning this event for more details). The method detailed here leads to the determination of a physical RSTF, the quality of which can be estimated by reconvolution with the EGF. We will select the best quality RSTFs for the global inversion process.

4 INVERSE METHOD: NEIGHBOURHOOD ALGORITHM

The expression we aim to minimize is the weighted sum of the misfit to the three types of data we use: *P*-wave displacements (noted U^P), *SH*-wave displacements (noted U^S), and RSTFs coming from the EGF analysis of surface waves (noted F_θ). We use the L1 norm for its robustness and the global misfit can then be written:

$$
\text{Misfit} = \sum_{i_P=1}^{n_P} \int_{t_P}^{t_P+D_P} \left| U_{i_P}^P(t) - \tilde{U}_{i_P}^P(t) \right| dt
$$
$$
+ W_S \sum_{i_S=1}^{n_S} \int_{t_S}^{t_S+D_S} \left| U_{i_S}^S(t) - \tilde{U}_{i_S}^S(t) \right| dt
$$
$$
+ W_{\text{surf}} \sum_{i_{\text{surf}}=1}^{n_{\text{surf}}} \int_{-\infty}^{\infty} \left| F_{\theta,i_{\text{surf}}}(t) - \tilde{F}_{\theta,i_{\text{surf}}}(t) \right| dt, \tag{14}
$$

where, t_P and t_S are the arrival times of *P* and *S* waves, and D_P and D_S are the duration we model for each of these waves. The ˜ symbol denotes the computed displacements. n_P, n_S, and n_{surf} are respectively the number of stations we use for each data set. Finally, W_S and W_{surf} denote the relative weight of *SH*-wave displacement and RSTFs, compared to the *P*-wave displacement. The *SH* weight compared to *P* waves is basically an amplitude normalization. The weighting for the RSTFs is more difficult to define, because they are a completely different type of information. Yet, we also consider a weight based on the relative amplitude between the RTSFs and the averaged *P*-wave amplitude. *A posteriori*, we checked that the misfit is approximately equilibrated between the different data we used, which indicates that the inversion is not dominated by part of the data.

Minimization of eq. (14), as a function of the kinematic parameters we have defined in Section (3.2), will allow us to define the possible source processes of the earthquake.

The way in which the problem is defined limits the number of parameters (at most 11), but it also makes the inverse problem very non-linear, with different local minima. Rather than trying to linearize the problem which would probably lead to a local minimum; we prefer to do a direct investigation of the parameter space. Because a completely random search is impossible in such high dimension spaces, a directed search must be used, belonging to the same class as simulated annealing or genetic algorithms. These two algorithms have been used in recent years in different areas of geophysics (e.g. Stoffa & Sen 1991; Gibert & Virieux 1991; Ihmlé 1996) when the problem becomes non-linear. Nevertheless, Sambridge (1999) and Lomax & Snieder (1994) have shown that in highly non-linear prob-

lems, even genetic algorithms are not exploratory enough to escape local minima.

This is why, here, we use the neighbourhood algorithm (NA) developed by Sambridge (1999). All the details are presented in Sambridge's paper, and we just recall here the main ideas of the algorithm. When we calculate the fit corresponding to a certain combination of the model parameters (represented by a point in the parameter space), we assume, as a first approximation, that the fit is the same in the neighbourhood of this point. Therefore, by choosing *n* points and drawing their neighbourhood cells (Voronoi 1908), it is possible to represent an approximation of the misfit function in the whole parameter space. It should be remembered that there are several useful properties of these cells: they can be defined in a space of all dimensions; and are unique and define a convex, space filling, pavement of the space.

The idea of Sambridge is to use the properties of these cells in an inversion scheme. Two parameters must be defined: the number of models considered at each iteration, called n_s; and the number of Voronoi cells in which we randomly select the n_s models, called n_r. Then, if we consider one iteration *j*, we calculate the fit for n_s models randomly chosen in n_r cells, and keep for the iteration $(j+1)$ the n_r cells defined by the n_r best points (in terms of misfit) generated so far. When the number of iterations increases, we are sampling, with increasing precision, the interesting parts of the parameter space as illustrated by the fig. 1 of Sambridge's paper. It is important to note that this algorithm is not easily trapped in a local minimum because a Voronoi cell is not fixed but evolves when the number of points increases. Moreover we can choose a more or less exploratory algorithm by increasing or decreasing the only two parameters n_s and n_r.

In the practical case of our slip-patch method, we use the following methodology: first, we test the one-patch model (10 inverted parameters), in which case we select (n_s, n_r) equal to (40, 25) and the total number of iterations equal to 150. Then, when we try to model an earthquake by two patches (11 inverted parameters), we run different inversions where the best angle α is searched by a grid search and the other parameters by a real inversion. In fact, direct inversion of α together with the other parameters makes the inversion unstable. In the two-patch model, NA is used with (n_s, n_r) equal to (120, 60) and a total number of iterations equal to 300. n_s and n_r have larger values than in the one-patch model to make the algorithm more exploratory, which is needed in this more complex case. To estimate the reliability of our results, we consider not only the best model given by NA but all the models which have a similar misfit. Thanks to the good sampling of the parameter space by NA, these models can be significantly different if the inverse problem is badly resolved. Moreover, we improve our appraisal of the results by using independent runs of NA. Finally, we obtain a good sampling of the possible good models allowing estimation of the means and standard deviations of the parameters by considering their marginal distributions (Ihmlé 1998).

5 MODELLING OF THE 1999 IZMIT (TURKEY) AND 1995 JALISCO (MEXICO) EARTHQUAKES

We propose to model two earthquakes which have been widely investigated in other studies. These two earthquakes illustrate the two main mechanisms candidates for a $M > 7$ earthquake, a strike slip continental and a subduction thrust earthquake. Source studies of the 1999 Izmit earthquake can be found in Delouis *et al.* (2002),

Yagi & Kikuchi (2000), Çakir *et al.* (2001), Bouchon *et al.* (2002) or Sekiguchi & Iwata (2002). Source studies of the 1995 Jalisco earthquake can be found in Courboulex *et al.* (1997a), Melbourne *et al.* (1997), Escobedo *et al.* (1998), Mendoza & Hartzell (1999) or McGuire *et al.* (2001).

5.1 The 1999 Izmit (Turkey) earthquake

5.1.1 Description

The Izmit earthquake caused significant devastation in western Turkey on 1999 August 17: at least 18 000 people were killed, and a lot of towns were almost completely destroyed. The causative fault is the western part of the North-Anatolian fault. Because of the gravity of the event itself, and the potential seismic risk for the town of Istanbul, this earthquake was extensively studied. We will later compare the insights brought by our approach with the results found by these studies.

We applied our method to determine the main features of the Izmit earthquake. The earthquake was well recorded by the broad-band stations of the IRIS-GEOSCOPE networks and we have selected 12 *P*- and 8 *SH*-wave records with a satisfactory azimuthal coverage (see Figs 4a and 5). A good candidate for an EGF analysis ($Mw =$ 5.8, *ca* 10 km east from the main shock hypocentre, with similar mechanism according to Harvard CMT), occurred on 1999 September 13 (Fig. 4b). We applied the projected Landweber method to all the IRIS-GEOSCOPE stations which recorded both events. The first part of our analysis concluded that a good approximation of the moment ratio between the main shock and the EGF is 350 (Harvard values give 480). We then constrain our deconvolution to respect this moment and we present in Fig. 6 the eight RSTFs we have selected for their quality. Because Love waves yield generally better RSTFs in this case, we have chosen to select only transverse component deconvolutions to avoid the use of different phase velocities in the inverse problem. Average phase velocity will be taken equal to 4.5 km s^{-1} (Schwartz 1999). The average of the durations of the RSTFs gives the absolute duration of the earthquake, which is here approximately equal to 18 s. Inversion will aim to simultaneously fit these RSTFs, the first 36 s of the *P*-wave displacement and the first 48 s of the *SH*-wave displacement. Periods longer than 80 s, and shorter than 4.5 s, which correspond to one-fourth of the global duration, are not considered in the inversion.

5.1.2 Results of our analysis

We present in Fig. 7 the results for the one-patch model. The mean and standard error values are evaluated by the marginal distributions given by a number of good models. Namely, we use 110 models coming from the 11 best models of 10 independent runs of NA. The fits obtained with the typical model of Fig. 7 are presented in Fig. 5 for body waves and in Fig. 6 for the RSTFs. The earthquake is satisfactorily modelled even with this simple representation and we consider that the addition of any complication (i.e. another patch) is not useful. Our defined mechanism (pure strike slip on a vertical east–west fault) is consistent with the various observations and modellings of this earthquake and the 15 km hypocentral depth is also comparable with the one inferred from local data (Toksöz *et al.* 1999). We find that the Izmit main rupture zone is a surface of approximately 70 km long and 15–20 km depth. Average slip is approximately 5–6 m and mean rupture velocity 2.3 km s^{-1}. Rupture is globally bilateral even if a slightly larger extension in the eastward direction is found by several inversion runs. These findings are consistent with the main common features of the other detailed kinematic studies (see
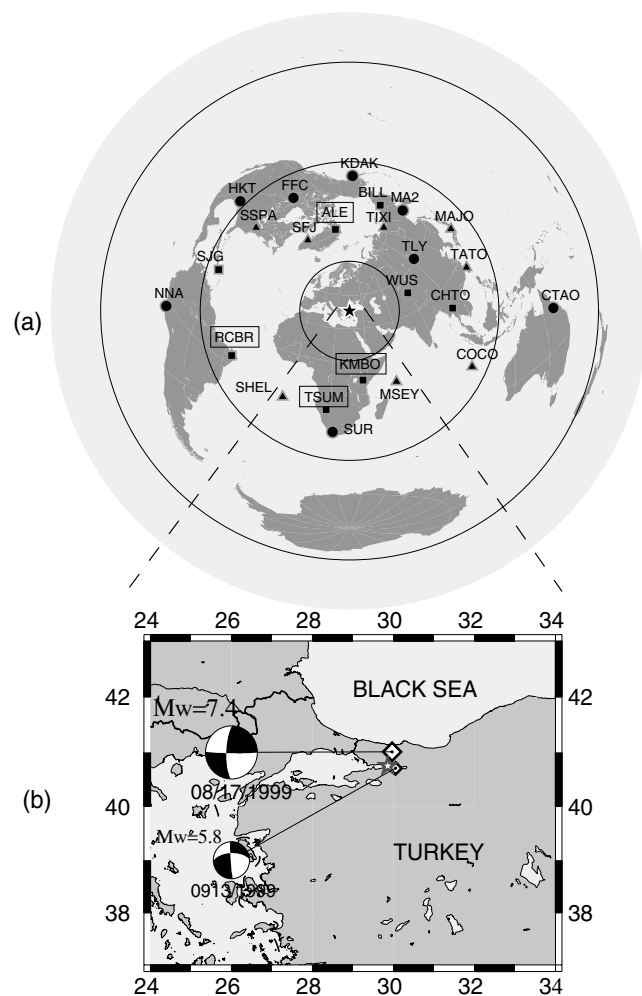

Figure 4. (a) Selected stations for the Izmit earthquake. The stations used for *P* waves, *SH* waves and surface waves (EGF analysis) are designed by triangles, squares, and circles respectively. Framed stations are those from which both *P* and *SH* waves are used. The large circles correspond to epicentral distances equal to 30°, 90°, and 150°. (b) Local map of the earthquake area, showing the magnitude, location and focal mechanism differences between the main shock and the EGF. The diamonds represent the location of the centroids as defined by Harvard CMT, whereas the star represents the main shock epicentre location as defined by NEIC.

Fig. 1). Delouis *et al.* (2002), Çakir *et al.* (2001), Bouchon *et al.* (2002), Yagi & Kikuchi (2000) all identified a 60–80 km long central moment release zone and typical slip values between 4 and 7 m. Slip in the eastern part of the fault (70 km east of the hypocentre) is less well constrained and more dependent on the studies. We find that the presence of a high slip at this location is not clearly required by the data we used. The slip patch that we obtain covers the zone where large surface slip occurred during the earthquake (Barka *et al.* 2002; Michel & Avouac 2002).

The obtained rupture velocity is lower than in most studies and particularly the one of Bouchon *et al.* (2002) who identified supershear rupture velocity on the eastern segment of the fault. Yet, it is important to remember that we do not allow for long rise times and complicated local source time functions and thus, we impose that the moment release occurs close to the rupture front, which may be not always the case. In fact, we identify an apparent rupture velocity, which is a lower bound of the real rupture velocity. In this
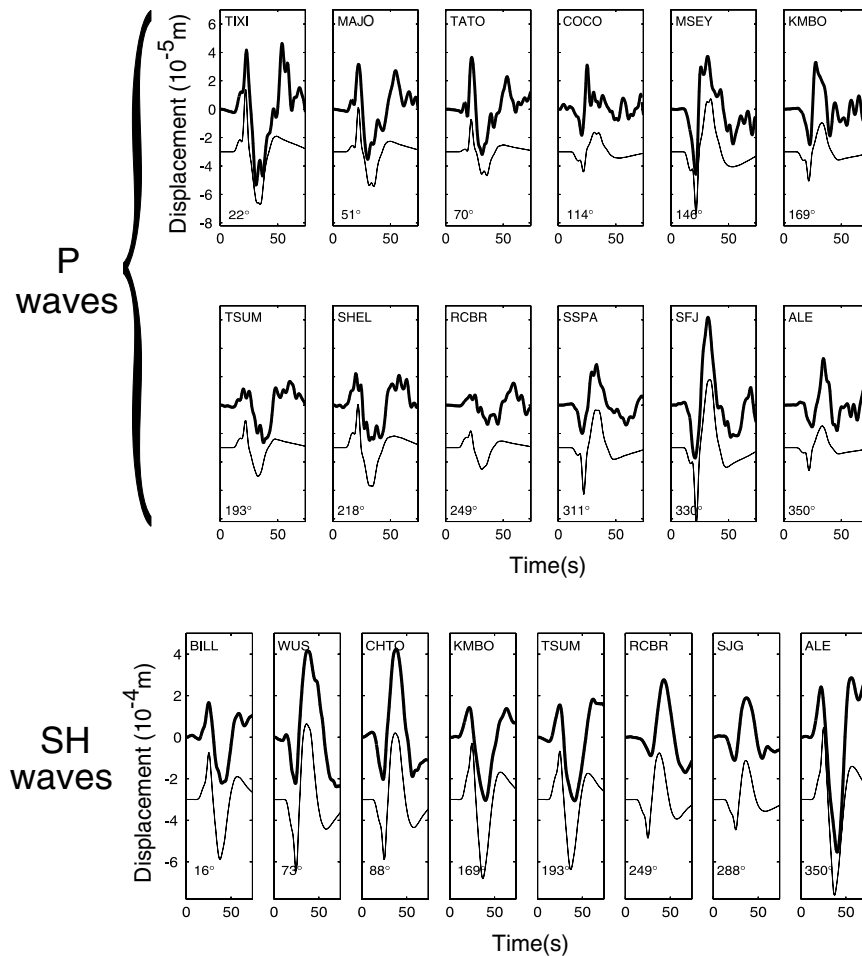
Figure 5. Body waves analysis of the Izmit earthquake. The 12 selected *P* waveforms are plotted in the upper part of the figure. The thick lines are the data, whereas the thin lines are the synthetics related to the model of Fig. 7. Names and azimuths of the stations are specified inside each subfigure. The eight selected *SH* waves are presented in a similar way in the lower part of the figure. Both *P* and *SH* waves have been bandpass filtered between 4.5 and 80 s (Butterworth filter).

sense, the obtained rupture velocity is consistent with the study of Delouis *et al.* (2002) (see fig. 17 of their study) where we can see that the apparent rupture velocity is around 2 km s^{-1}, whereas the real rupture velocity is higher. Nevertheless, we find some clues indicative of a high rupture velocity in the eastern direction: we cannot fit the very impulsive initial parts of the RSTFs at stations TLY and CTAO (Fig. 6).

To improve the agreement with data, we have tried to make the source more complex with the addition of a second patch. We have found that no significant improvement is obtained. We do not consider that site effects have a large contribution here because the largest differences concern the EGF analysis, which is not directly influenced by such effects. Rather, we consider that complex source effects exist and that the attainment of a better model would require the complete description of the kinematic behaviour of each point of the fault. This is not the purpose of the study, which aims to extract only the main and robust features of the earthquake.

5.2 The 1995 Jalisco (Mexico) earthquake

5.2.1 Description

On 1995 October 9, a very large thrust earthquake ($Mw = 7.9$–8.) occurred in the Mexican subduction zone, in front of the town of Jalisco. The earthquake caused the death of at least 49 people and

was also responsible for a substantial tsunami (Ortiz *et al.* 1998). Aftershocks lie on a 70 km × 170 km (along trench) surface (Pacheco *et al.* 1997). The earthquake was well recorded by the broad-band stations of the IRIS-GEOSCOPE networks and we have selected 12 *P*- and 8 *SH*-wave records with a satisfactory azimuthal coverage (Figs 8a and 9). This earthquake was preceded and followed by two $M = 6$ events, both of which allow an EGF analysis of the main shock (Courboulex *et al.* 1997a). We selected the 1995 October 12 event as the EGF for our subsequent analysis. Fig. 8(b) illustrates the main characteristics of this EGF compared to the main shock.

We begin with the EGF analysis because it requires few hypotheses on the main shock source process. We first use Bertero's method (which does not constrain the relative moment between main shock and the EGF). Based on the results found for the best deconvolutions, we evaluate this relative moment to 450 (Harvard CMT values give 1095). Thus, we constrain the deconvolutions to this value and the selected RSTFs are presented in Fig. 10. The global duration of the event can be estimated to 60 s by the average of the apparent durations. A clear directivity effect can be seen on the RSTFs: they have a much longer duration and a lower amplitude in the southeastern direction (station SDV) than in the northwestern direction (stations GUMO, MAJO, SCZ). We now propose to quantitatively model these RSTFs, simultaneously with the body waves, by our
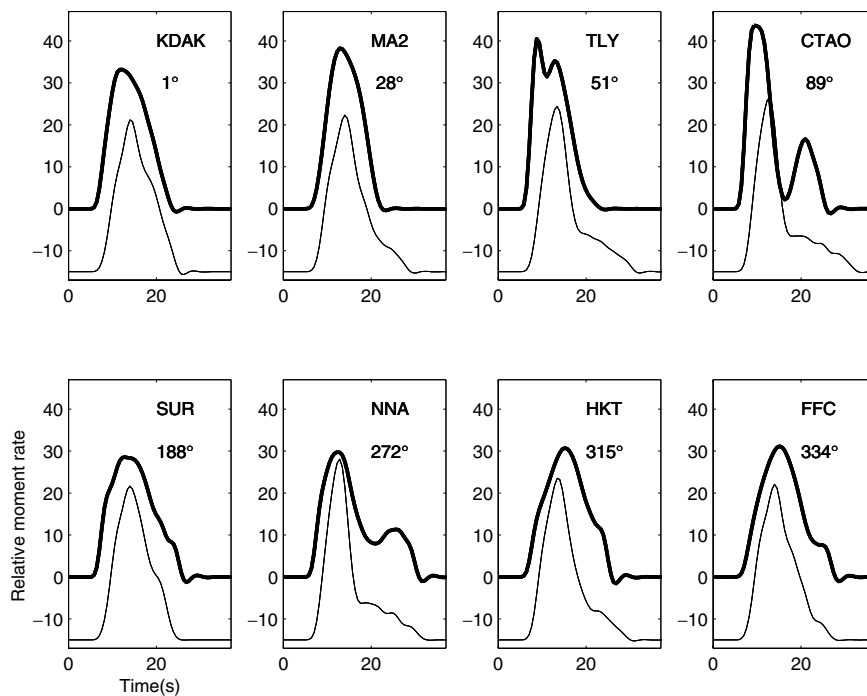
Figure 6. Surface waves analysis of the Izmit earthquake. The thick lines are the real RSTFs, that is the RSTFs obtained by our constrained deconvolution for Love waves. The thin lines are synthetics related to the model of Fig. 7. The origin times of the RSTFs are fixed at $t = 5$ s. Names and azimuths of the stations are specified inside each subfigure. Data and synthetics have been low-pass filtered at 4.5 s (Butterworth filter).
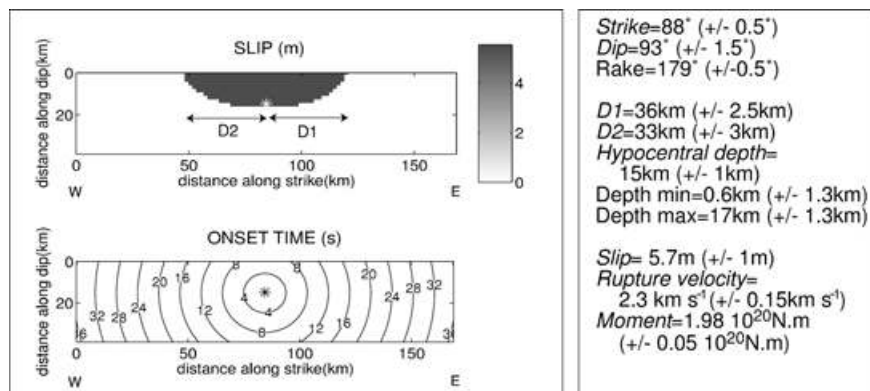

Figure 7. Results of the one-patch modelling of the Izmit earthquake. Typical slip and onset times distributions are respectively reproduced in the upper and lower part of the figure. In both figures, the hypocentre is denoted by a star. We also present the mean and standard error values on different rupture parameters (see the definition of D1, D2 in the upper figure). These values are obtained by the analysis of 110 models, coming from the 11 best models of 10 independent runs of the NA.

slip-patch method. Here, we have used both Rayleigh and Love waves to improve the azimuthal coverage, and we are averaging the phase velocities of these waves to 3.8 km s^{-1} and 4.5 km s^{-1}, respectively. We model the first 110 s of the P-wave displacement and the first 140 s of the SH-wave displacement. Periods longer than 80 s, and shorter than 20 s, which corresponds to one-third of the global duration, are not considered in the inversion.

5.2.2 Results of our analysis

We first describe the results inferred by the one-patch model. Because some coherent features of the waveforms cannot be modelled with this simple approach, we add another patch and show in this case that the global agreement with the data is significantly improved.

(i) One-patch model
Fig. 11 describes the results obtained by this simple modelling. As for the Izmit earthquake, estimation of the means and standard errors comes from the marginal distributions of 110 good models. The fits obtained with the typical model of Fig. 11 are presented in Fig. 9 for body waves and in Fig. 10 for the RSTFs. A large part of the data is explained with this simple unilateral model. Slip is found to occur at shallow depths which is consistent with the studies of Melbourne *et al.* (1997) and Mendoza & Hartzell (1999) and with the substantial generated tsunami. The rupture length (160 km) has to be compared with the 120 km found by Escobedo *et al.* (1998) or McGuire *et al.* (2001), the 150 km found by Courboulex *et al.* (1997a) and the 170 km long aftershock zone inferred by Pacheco *et al.* (1997). Rupture velocity (2.6 km s^{-1}) is between the 2.2 km s^{-1} obtained by Escobedo *et al.* (1998) and the 2.8 km s^{-1} obtained by
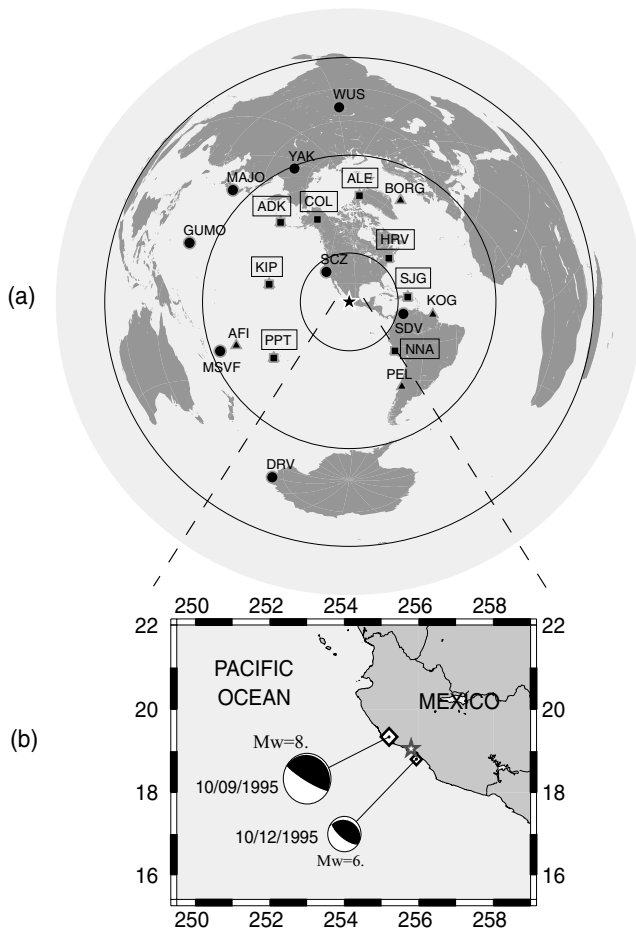
Figure 8. (a) Selected stations for the Jalisco earthquake. The stations used for *P* waves, *SH* waves and surface waves (EGF analysis) are designed by triangles, squares, and circles respectively. Framed stations are those from which both *P* and *SH* waves are used. The large circles correspond to epicentral distances equal to 30°, 90°, and 150°. (b) Local map of the earthquake area, showing the magnitude, location and focal mechanism differences between the main shock and the EGF. The diamonds represent the location of the centroids as defined by Harvard CMT, whereas the star represents the main shock epicentre location as defined by NEIC.

Courboulex *et al.* (1997a). The mean slip (3 m) is consistent with the typical slip values of the inversions of Melbourne *et al.* (1997) and Mendoza & Hartzell (1999). Yet, we notice that an important and coherent pulse of the *P* waveforms is not well modelled (see Fig. 9, at a time *ca* 70 s). This observation leads us to refine this simple model, by adding another patch. In this second step, we keep the values of the focal mechanism (strike = 300°; dip = 25°; rake =93°) and of the hypocentral depth (20 km) that we have inferred here.

(ii) Two-patch model
Fig. 12 shows a typical model obtained by this modelling as well as the uncertainties on slip and rupture velocity distributions. The fits obtained with this model are presented in Fig. 13 for body waves and in Fig. 14 for the RSTFs. Agreement with the latter part of *P*-wave displacement is clearly improved by the addition of the second patch. Variance reductions, which were about 58 per cent for *P* waves and 83 per cent for *SH* waves with the one-patch model, are now equal to 67 per cent for *P* waves and 86 per cent for *SH* waves. The fit to RSTFs, which is more difficult to express in terms of variance reduction, is also improved. Thus, it is well resolved that this rupture complication is needed in the northwestern part of the fault. Yet, in

Fig. 12(e) and (f), we can see from the standard errors that this part of the rupture can be modelled by different kinematic scenarios. In fact, among the models with similar fit to the data, the most frequent one is the typical model we present in Fig. 12: a zone with smaller slip, smaller rupture velocity, and larger extension in the downdip direction. Nevertheless, other models, for example with a smaller zone and higher rupture velocity, are also possible.

This rupture complexity is consistent with other studies of the Jalisco earthquake. Courboulex *et al.* (1997a) have shown by an inverse Radon transform, that the earthquake kinematics becomes more complex in the last 20 s of the rupture. Mendoza & Hartzell (1999) have proposed a model with an excellent fit to teleseismic *P* waves in which complex local source time functions are required at the end of the rupture.

6 DISCUSSION AND CONCLUSION

This paper presents a method to estimate reliably the large-scale features of the earthquake rupture. The simplicity of the source description, as well as the variety of modelled data (*P*, *SH* and surface waves), reduces the instability of this classical inverse problem. The aim of this slip patch method is not to infer the precise rupture scenario, a very difficult problem which requires a large number of near-field stations, but to obtain the following types of results: location and size of the main moment release zone(s), mean slip, and mean rupture velocity. This approach is intermediary between centroid models and a real source tomography. It also offers an easier comparison with the earthquake reality than the second moments analysis of the moment tensor. This approach allows control of the inverse problem and an estimation of which features of the slip distribution are really needed to explain the data. We begin the analysis by using only one patch and we complicate the model only if it is necessary. By such a procedure, a simple kinematic model is identified and unnecessary features are not introduced into the source model.

In this study, body waves are analysed in a classical way: we directly model the first tenths of seconds of *P* and *SH* displacements. On the contrary, for surface waves, we are proposing a development of the well-known EGF technique. Starting from Bertero's projected Landweber method (Bertero *et al.* 1997), we impose the physical constraint that the area of the RSTFs have to be the same at all stations, and that this value is equal to the moment ratio between the main shock and the EGF. This physical constraint has the double advantage of stabilizing the deconvolutions and allowing an easier comparison with synthetics. More details about this technique can be found in Vallée (2004).

Finally, this method does not require much processing and the data needed are easily available soon after the earthquake thanks to the global networks. Only the EGF analysis is not completely straightforward. A suitable EGF may not always be available, as for the 2001 January 26 India earthquake. On the contrary, when several EGF are available, which is often the case for subduction earthquakes, it may be useful to test these different possibilities. Yet, this approach allows a quasi-systematic study of large earthquakes and thus offers the possibility to look for global features of the earthquake rupture. In parallel, it can be used for near-real-time reports of the main features of the rupture process. This is particularly important in the identification of the size and the location of the zone affected by an earthquake. Another ambitious goal would be to use such a study for tsunami alerts. In fact, our modelling is potentially able to identify shallow slip and/or slow rupture velocity which
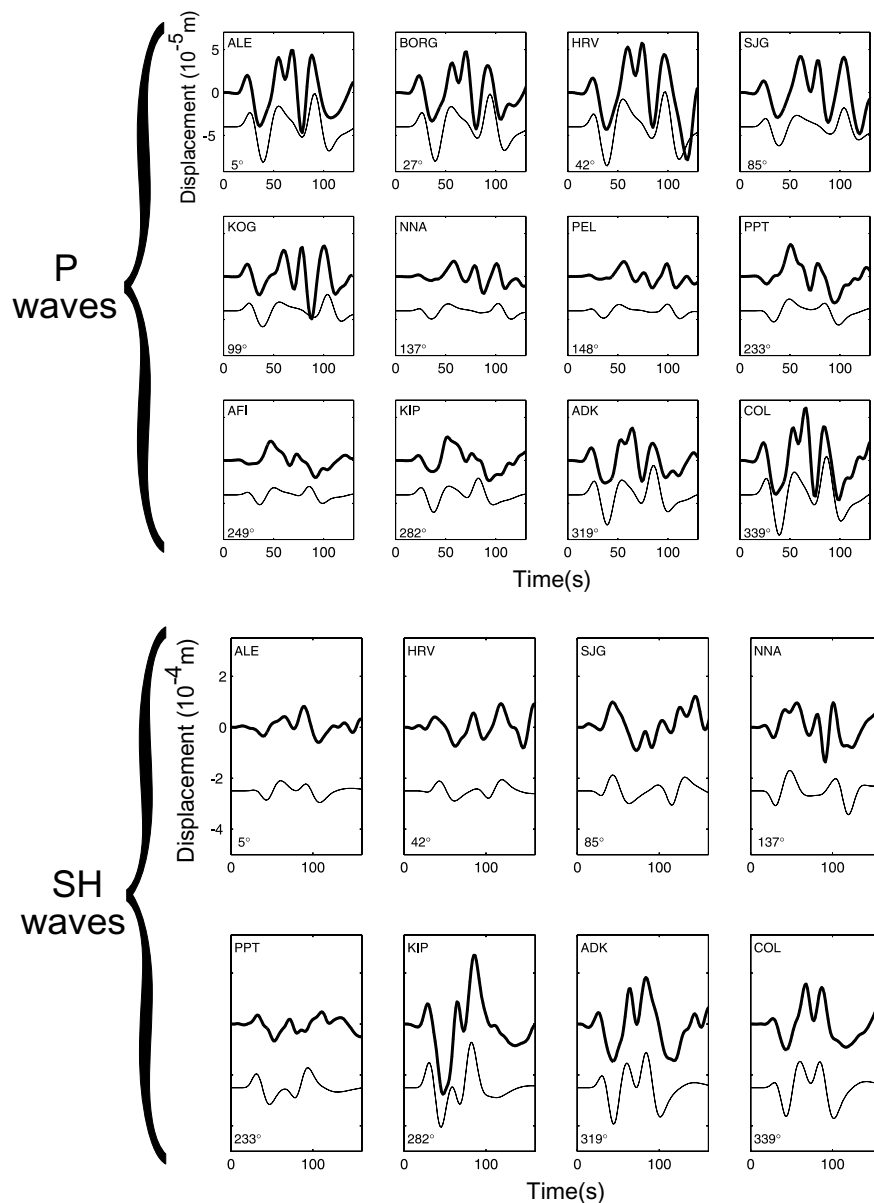
Figure 9. Body waves analysis of the Jalisco earthquake (one-patch model). The 12 selected *P* waveforms are plotted in the upper part of the figure. The thick lines are the data whereas the thin lines are the synthetics related to the one-patch model of Fig. 11. Names and azimuths of the stations are specified inside each subfigure. The eight selected *SH* waves are presented in a similar way in the lower part of the figure. Both *P* and *SH* waves have been bandpass filtered between 20 and 80 s (Butterworth filter).

are indicators of the destructive tsunami earthquakes. Today, only the Earthquake Research Institute (ERI 2002) provides a complete kinematic inversion of the source process typically one or two days after the earthquake. Their inversion, which uses only body waves, is based on a classical subfault discretization of the fault plane. Our method, which uses more data and looks for larger-scale features of the source process may yield less detailed but more robust results.

REFERENCES

Abercrombie, R.A., Antolik, M., Felzer, K. & Ekström, G., 2001. The 1994 Java tsunami earthquake: Slip over a subducting seamount, *J. geophys. Res.,* **106,** 6595–6607.
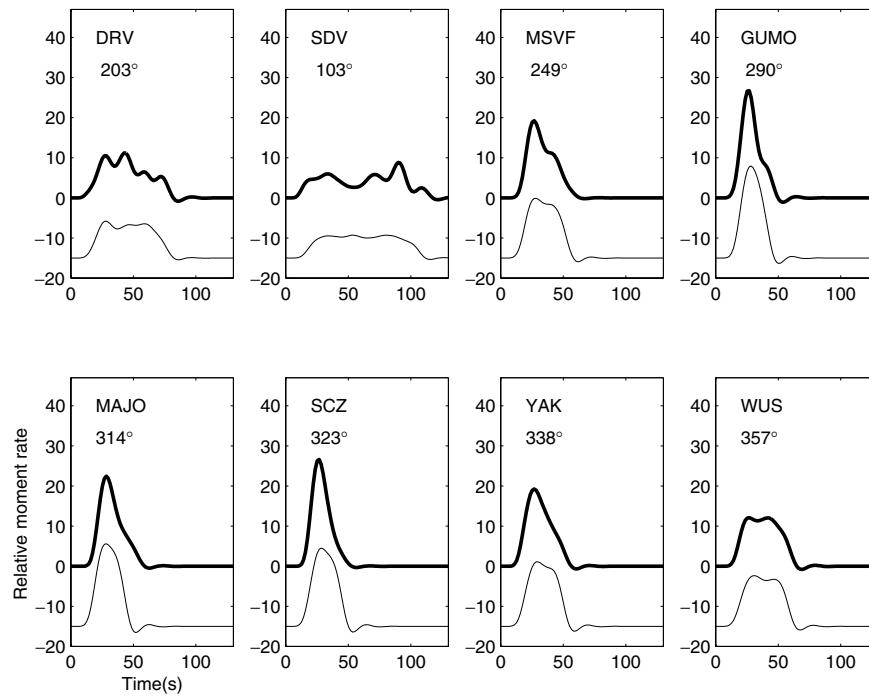
Figure 10. Surface waves analysis of the Jalisco earthquake (one-patch model). The thick lines are the real RSTFs, that is the RSTFs obtained by our constrained deconvolution. The thin lines are synthetics related to the model of Fig. 11. The origin times of the RSTFs are fixed at $t = 5\,s$. Names and azimuths of the stations are specified inside each subfigure. Data and synthetics have been low-pass filtered at 20 s (Butterworth filter).
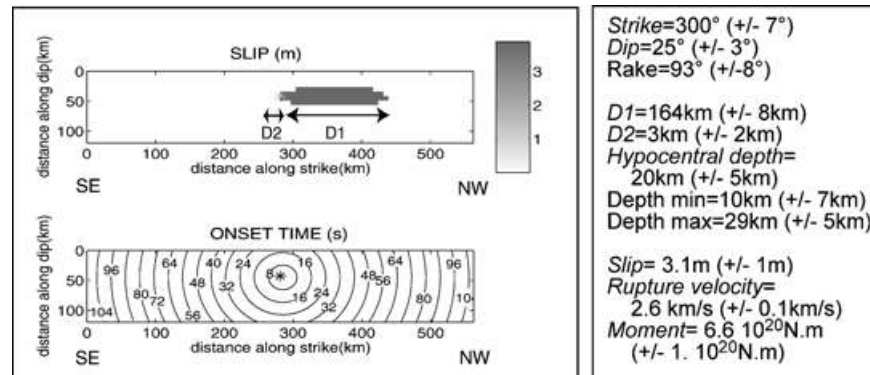

Figure 11. Results of the one-patch modelling of the Jalisco earthquake. Typical slip and onset times distributions are reproduced in the upper and lower part of the figure respectively. In both figures, the hypocentre is denoted by a star. We also present the mean and standard error values on different rupture parameters (see the definition of D1, D2 in the upper figure). These values are obtained by the analysis of 110 models, coming from the 11 best models of 10 independent runs of the NA.

Archuleta, R.J., 1982. Analysis of near-source static and dynamic measurements from the 1979 Imperial Valley earthquake, *Bull. seism. Soc. Am.,* **72,** 1927–1956.

Backus, G.E., 1977. Interpreting the seismic glut moments of total degree two or less, *Geophys. J. R. astr. Soc.,* **51,** 1–25.

Barka, A. *et al.*, 2002. The surface rupture and slip distribution of the 17 August 1999 Izmit earthquake (M 7.4), North Anatolian fault, *Bull. seism. Soc. Am.,* **92,** 43–60.

Bertero, M., Bindi, D., Boccacci, P., Cattaneo, M., Eva, C. & Lanza, V., 1997. Application of the projected Landweber method to the estimation of the source time function in seismology, *Inverse Problems,* **13,** 465–486.

Bouchon, M., Teleseismic body wave radiation from a seismic source in a layered medium, *Geophys. J. R. astr. Soc.,* **47,** 515–530.

Bouchon, M., Toksoz, N.M., Karabulut, H., Bouin, M.P., Dietrich, M., Aktar, M. & Edie, M., 2002. Space and time evolution of rupture and faulting during the 1999 Izmit (Turkey) earthquake, *Bull. seism. Soc. Am.,* **92,** 256–266.

Bukchin, B.G., 1995. Determination of stress glut moments of total degree 2 from teleseismic surface wave amplitude spectra, *Tectonophysics,* **248,** 185–191.

Çakir, Z., De Chabalier, J.B., Armijo, A., Meyer, B., Barka, A. & Peltzer, G., 2001. *The August 17, 1999, Turkey, earthquake seen with InSAR imagery and tectonic field observations,* EUG XI Meeting, Strasbourg, France.

Clévédé, E., Bouin, M.-P., Bukchin, B., Mostinskiy, A. & Patau, G., 2004. New constraints on the rupture process of the 1999 August 17 Izmit earthquake deduced from estimates of stress glut note moments, *Geophys. J. Int.,* in press.

Courboulex, F., Singh, S.K., Pacheco, J.F. & Ammon, C.J., 1997a. The 1995 Colima-Jalisco, Mexico, earthquake (Mw 8): a study of the rupture process, *Geophys. Res. Lett.,* **24,** 1019–1022.

Courboulex, F., Santoyo, M.A., Pacheco, J.F. & Singh, S.K., 1997b. The 14 September 1995 (*M* = 7.3) Copala, Mexico, earthquake: a source study using teleseismic, regional, and local data, *Bull. seism. Soc. Am.,* **87,** 999–1010.
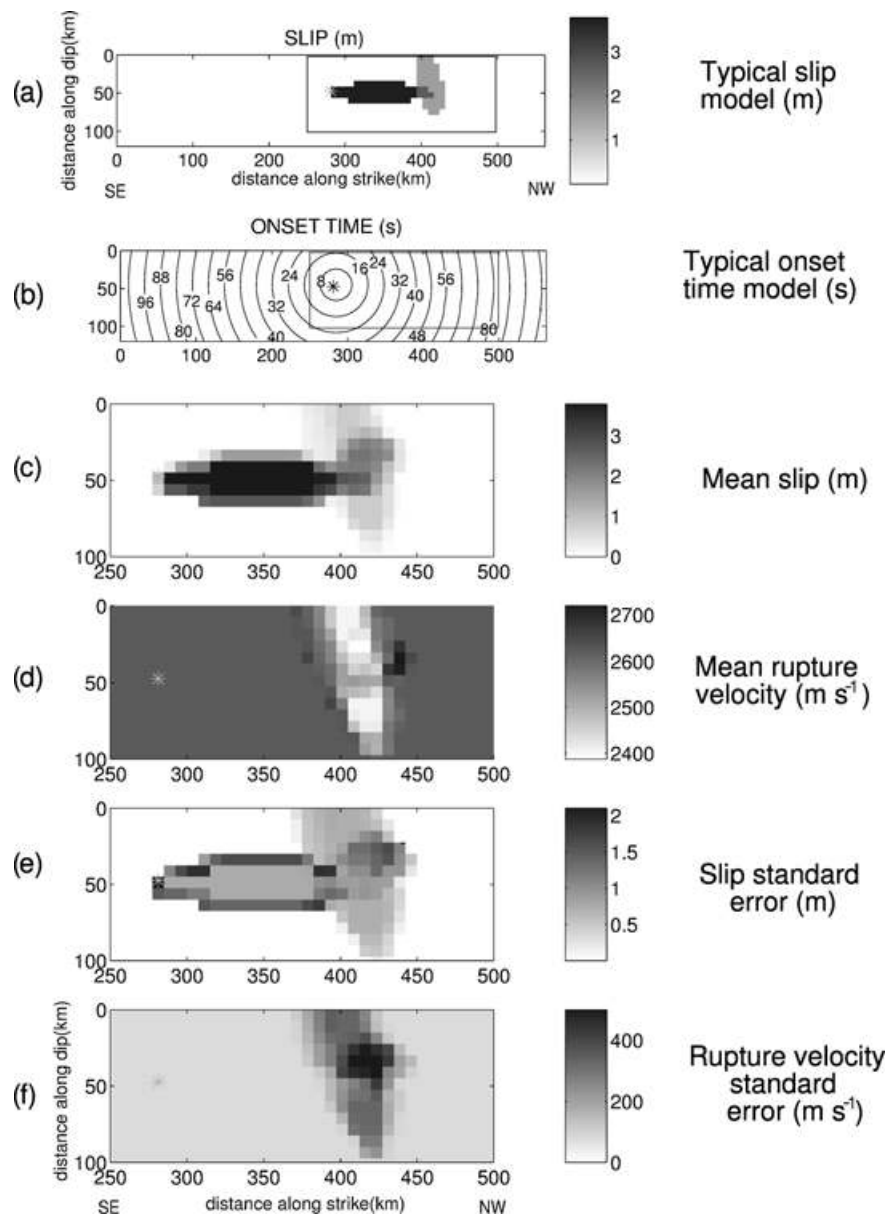
Figure 12. Results of the two-patch modelling of the Jalisco earthquake. (a) and (b) A typical model, with its slip and onset time distribution, is first represented. Hypocentre is denoted by the star. (c), (d), (e), and (f) Statistical variations of slip and rupture velocity distributions. These values are obtained by the analysis of 110 models, coming from the 11 best models of 10 independent runs of the NA. Only the part of the fault corresponding to the boxes in (a) and (b) is reproduced.

Dahm, T. & Krüger, F., 1999. Higher degree moment tensor inversion using far-field broad-band recordings: I). Theory and evaluation of the method with application to the Bolivia deep earthquake, *Geophys. J. Int.,* **137,** 35–50.

Das, S. & Kostrov, B.V., 1990. Inversion of seismic slip rate history and distribution with stabilizing constraints: application to the 1986 Andreanof Islands earthquake, *J. geophys. Res.,* **95,** 6899–6913.

Das, S. & Kostrov, B.V., 1994. Diversity of solutions of the problem of earthquake faulting inversion; application to *SH* waves for the great 1989 Macquarie Ridge earthquake, *Phys. Earth planet. Int.,* **85,** 293–318.

Das, S. & Suhadolc, P., 1996. On the inverse problem for earthquake rupture: the Haskell-type source model, *J. geophys. Res.,* **101,** 5725–5738.

Delouis, B., Giardini, D., Lundgren, P. & Salichon, J., 2002. Joint inversion of InSAR, GPS, teleseismic, and strong-motion data for the spatial and temporal distribution of earthquake slip: application to the 1999 Izmit mainshock, *Bull. seism. Soc. Am.,* **92,** 278–299.

Dziewonski, A.M., Chou, T.A. & Woodhouse, J.H., 1981. Determination of earthquake source parameters from waveform data for studies of global and regional seismicity, *J. geophys. Res.,* **86,** 2825–2852.

ERI, Earthquake Research Institute, 2002. *Earthquake and volcano*, http://www.eri.u-tokyo.ac.jp/, Tokyo, Japan.

Escobedo, D., Pacheco, J.F. & Suarez, G., 1998. Teleseismic body-wave analysis of the 9 October, 1995 (M_W = 8.0), Colima-Jalisco, Mexico earthquake, and its largest foreshock and aftershock, *Geophys. Res. Lett.,* **25,** 547–550.

Fukao, Y., 1972. Source process of a large deep-focus earthquake and its tectonic implications-The western Brazil earthquake of 1963, *Phys. Earth planet. Int.,* **5,** 61–76.

Gibert, D. & Virieux, J., 1991. Electromagnetic imaging and simulated annealing, *J. geophys. Res.,* **96,** 8057–8067.

Hartzell, S.H., 1978. Earthquake aftershocks as Green's functions, *Geophys. Res. Lett.,* **5,** 1–4.
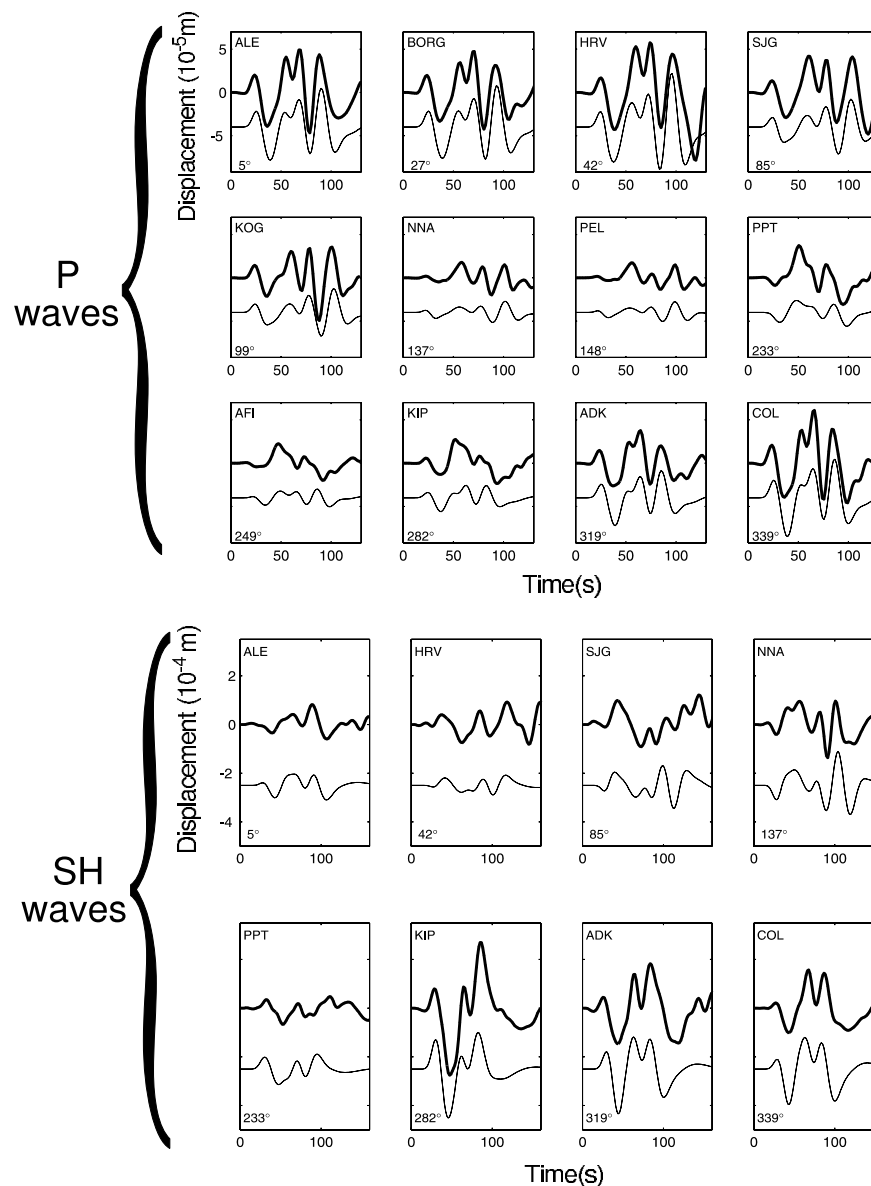
Figure 13. Body waves analysis of the Jalisco earthquake (two-patch model, Fig. 11). Same notations as in Fig. 9. Note that the latter part of the seismograms is clearly better modelled with two patches, particularly for *P* waves.

Hartzell, S.H. & Heaton, T.H., 1983. Inversion of strong ground motion and teleseismic waveform data for the fault rupture history of the 1979 Imperial Valley, California, earthquake, *Bull. seism. Soc. Am.,* **73,** 1553–1583.

Hernandez, B., Cotton, F. & Campillo, M., 1999. Contribution of radar interferometry to a two-step inversion of the kinematic process of the 1992 Landers earthquake, *J. geophys. Res.,* **104,** 13 083–13 099.

Herrero, A., 1994. Space-time and spectral parameterisation of seismic sources and its application to seismic hazard, *Ph.D. thesis*, IPGP, Paris, France.

Ihmlé, P.F., 1996. Monte Carlo slip inversion in the frequency domain: application to the 1992 Nicaragua slow earthquake, *Geophys. Res. Lett.,* **23,** 913–916.

Ihmlé, P.F. & Ruegg, J.C., 1997. Source tomography by simulated annealing using broad-band surface waves and geodetic data: application to the $M_w = 8.1$ Chile 1995 event, *Geophys. J. Int.,* **131,** 146–158.

Ihmlé, P.F., 1998. On the interpretation of subevents in teleseismic waveforms: the 1994 Bolivia deep earthquake revisited, *J. geophys. Res.,* **103,** 17 919–17 932.

Kikuchi, M. & Kanamori, H., 1982. Inversion of complex body waves, *Bull. seism. Soc. Am.,* **72,** 491–506.

Lomax, A. & Snieder, R., 1994. Finding sets of acceptable solutions with a genetic algorithm with application to surface wave group dispersion in Europe, *Geophys. Res. Lett.,* **21,** 2617–2620.

Ma, K.F., Song, T.R.A., Lee, S.J. & Wu, H.I., 2000. Spatial slip distribution of the September 20, 1999, Chi-Chi, Taiwan, earthquake ($M_w = 7.6$)-inverted from teleseismic data, *Geophys. Res. Lett.,* **27,** 3417–3420.

Ma, K.F., Mori, J., Lee, S.J. & Yu, S.B., 2001. Spatial and Temporal distribution of slip for the 1999 Chi-Chi Taiwan earthquake, *Bull. seism. Soc. Am.,* **91,** 1069–1087.

Massonnet, D., Rossi, M., Carmona, C., Adragna, F., Peltzer, G., Feigl, K. & Rabaute, T., 1993. The displacement field of the Landers earthquake mapped by radar interferometry, *Nature,* **364,** 138–142.

McGuire, J.J., Li Zhao & Jordan, T.H., 2001. Teleseismic inversion for the second-degree moments of earthquake space-time distributions, *Geophys. J. Int.,* **145,** 661–678.

Melbourne, T., Carmichael, I., Demets, C., Hudnut, K., Sanchez, O., Stock, J., Suarez, G. & Webb, F., 1997. The geodetic signature of the
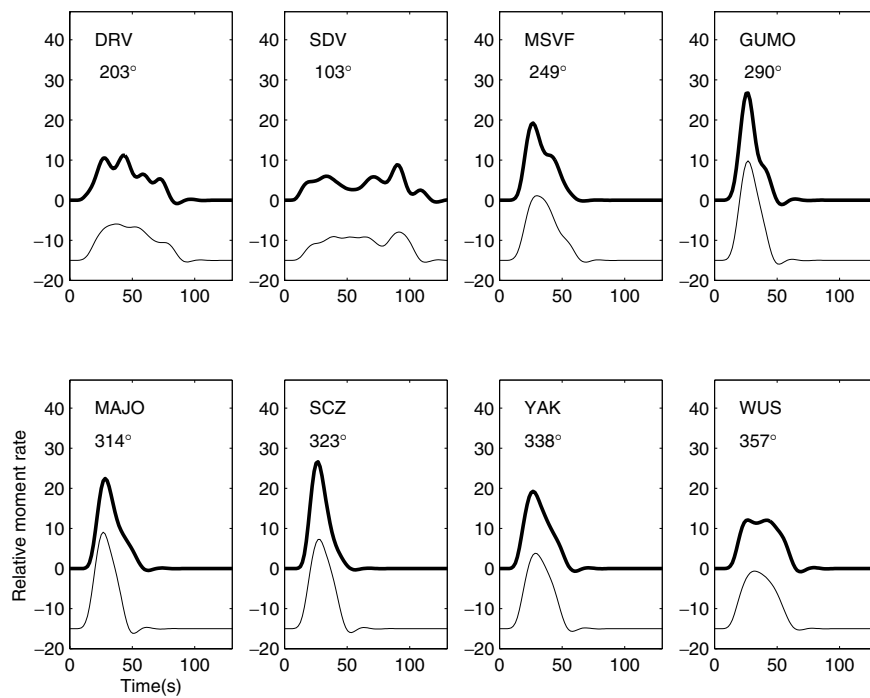
Figure 14. Surface waves analysis of the Jalisco earthquake (two-patch model, Fig. 11). Same notations as in Fig. 10.

M8.0 Oct. 9, 1995, Jalisco subduction earthquake, *Geophys. Res. Lett.,* **24,** 715–718.

Michel, R. & Avouac, J.P., 2002. Deformation due to the 17 August 1999 Izmit Turkey, earthquake measured from SPOT images, *J. geophys. Res.,* **107,** 2062, doi: 10.1029/2000JB000102.

Mendoza, C. & Hartzell, S., 1999. Fault-slip distribution of the 1995 Colima-Jalisco, Mexico, earthquake, *Bull. seism. Soc. Am.,* **89,** 1338–1344.

Mooney, W.D., Laske, G. & Masters T.G., 1998. CRUST 5.1: a global crustal model at degrees *5 degrees, *J. Geophys. Res.,* **103,** 727–747, 1

Müller, G., 1985. The reflectivity method: a tutorial, *J. Geophys.,* **58,** 153–174.

Olson, A.H. & Apsel, R.J., 1982. Finite fault and inverse theory with applications to the 1979 Imperial Valley earthquake, *Bull. seism. Soc. Am.,* **72,** 1969–2001.

Ortiz, M., Singh, S.K., Pacheco, J. & Kostoglodov, V., 1998. Rupture length of the October 9, 1995 Colima-Jalisco earthquake ($M_W = 8$) estimated from tsunami data, *Geophys. Res. Lett.,* **25,** 2857–2860.

Pacheco, J. *et al.*, 1997. The October 9, 1995 Colima-Jalisco, Mexico earthquake ($M_W = 8$): an aftershock study and a comparison of this earthquake with those of 1932, *Geophys. Res. Lett.,* **24,** 2223–2226.

Podvin, P. & Lecomte, I., 1991. Finite difference computation of traveltimes in very contrasted velocity models: a massively parallel approach and its associated tools, *Geophys. J. Int.,* **105,** 271–284.

Sambridge, M., 1999. Geophysical inversion with a neighbourhood algorithm. I. Searching a parameter space, *Geophys. J. Int.,* **138,** 479–494.

Schwartz, S.Y., 1999. Noncharacteristic behavior and complex recurrence of large subduction zone earthquakes, *J. geophys. Res.,* **104,** 23 111–23 125.

Sekiguchi, H. & Iwata, T., 2002. Rupture process of the 1999 Kocaeli, Turkey, earthquake estimated from strong-motion waveforms, *Bull. seism. Soc. Am.,* **92,** 300–311.

Stoffa, P.L. & Sen, M.K., 1991. Nonlinear multiparameter optimization using genetic algorithms: Inversion of plane wave seismograms, *Geophysics,* **56,** 1794–1810.

Thatcher, W., 1990. Order and diversity in the modes of circum-Pacific earthquake recurrence, *J. geophys. Res.,* **95,** 2609–2623.

Toksöz, M.N., Reilinger, R.E., Doll, C.G., Barka, A.A. & Yalcin, N., 1999. Izmit (Turkey) earthquake of 17 August 1999: first report, *Seism. Res. Lett.,* **70,** 669–679.

Vallée, M., 2004. Stabilizing the empirical Green function analysis: development of the projected Landweber method, *Bull. Seism. Soc. Am.,* in press.

Vallée, M., Bouchon, M. & Schwartz, S.Y., 2003. The January 13, 2001 El Salvador earthquake: a multi-data analysis, *J. geophys. Res.,* **108,** 2203, doi:10.1029/2002JB001922.

Velasco, A.A., Ammon, C.J., Lay, T. & Jiajun-Zhang, 1994a. Imaging a slow bilateral rupture with broadband seismic waves: The September 2, 1992 Nicaraguan tsunami earthquake, *Geophys. Res. Lett.,* **21,** 2629–2632.

Velasco, A.A., Ammon, C.J. & Lay, T., 1994b. Empirical Green function deconvolution of broadband surface waves: rupture directivity of the 1992 Landers, California ($M_W = 7.3$), *Bull. seism. Soc. Am.,* **84,** 735–750.

Voronoi, M.G., 1908. Nouvelles applications des paramétres continusà la théorie des formes quadratiques, *J. reine Angew. Math.,* **134,** 198–227.

Wu, C., Takeo, M. & Ide, S., 2001. Source process of the Chi-Chi earthquake: a joint inversion of strong motion data and Global Positioning System data with a multifault model, *Bull. seism. Soc. Am.,* **91,** 1128–1143.

Yagi, Y. & Kikuchi, M., 2000. Source rupture process of the Kocaeli, Turkey, earthquake of August 17, 1999, obtained by joint inversion of near-field data and teleseismic data, *Geophys. Res. Lett.,* **27,** 1969–1972.

Zeng, Y. & Chen, C.H., 2001. Fault rupture process of the 20 september Chi-Chi, Taiwan, earthquake, *Bull. seism. Soc. Am.,* **91,** 1088–1098.